



2 DOCTORAL THESIS

4 Optimisation studies and background
5 estimation in searches for the supersymmetric
6 partner of the top quark in all-hadronic final
7 states with the ATLAS Detector at the LHC

9 *A thesis submitted in fulfillment of the requirements
10 for the degree of Doctor of Philosophy*

11 *in the*

12 Experimental Particle Physics Research Group
13 School of Mathematical and Physical Sciences

14 *Author:*
15 Fabrizio MIANO

Supervisor:
Dr. Fabrizio SALVATORE

14th October 2017

Dedicated to my family.

*Have no fear for atomic energy
'cause none of them can stop the
time*

17

Robert Nesta Marley

18

Acknowledgments

¹⁹ Thanks to every single thing that went wrong. It made me stronger.

Declaration

21 I, Fabrizio MIANO, hereby declare that this thesis, titled, "Optimisation studies and back-
22 ground estimation in searches for the supersymmetric partner of the top quark in all-
23 hadronic final states with the ATLAS Detector at the LHC" has not been and will not be,
24 submitted in whole or in part to another University for the award of any other degree.

25 *Brighton, June 2018*

University of Sussex
School of Mathematical and Physical Sciences
Experimental Particle Physics Research Group

Doctoral Thesis

31
32 Optimisation studies and background estimation in searches for
33 the supersymmetric partner of the top quark in all-hadronic final
34 states with the ATLAS Detector at the LHC

36 by Fabrizio MIANO

Abstract

38 This thesis presents searches for supersymmetry in $\sqrt{s} = 13$ TeV proton-proton collisions
39 at the LHC using data collected by the ATLAS detector in 2015, 2016 and 2017. Events
40 with 4 or more jets and missing transverse energy were selected. Kinematic variables
41 were investigated and optimisations were performed to increase the sensitivity to su-
42 persymmetric signals. Standard Model backgrounds were estimated by means of Monte
43 Carlo simulations and data-driven techniques. Before analysing the data in the blinded
44 signal regions the agreement between data and background predictions and the extrapol-
45 ations from control and validation regions to signal regions were validated. The analysis
46 yielded no significant excess in any of the analyses performed. Therefore limits were
47 set and the results were interpreted as lower bounds on the masses of supersymmetric
48 particles in various scenarios and models.

49 Contents

50	Introduction	1
51	1 The Standard Model, Supersymmetry, and the motivations behind it	2
52	1.1 The Standard Model	2
53	1.1.1 Overview	3
54	1.1.2 Limitations of the Standard Model	6
55	1.2 Supersymmetry	6
56	1.2.1 Why SUSY?	6
57	1.2.2 Minimal Supersymmetric Standard Model	6
58	1.2.3 R -parity SUSY	7
59	1.2.4 Simplified models	7
60	1.2.5 Phenomenological MSSM	7
61	2 The ATLAS Experiment at the LHC	8
62	2.1 The LHC	8
63	2.2 The ATLAS Detector	10
64	2.2.1 The Magnet System	12
65	2.2.2 The Inner Detector	13
66	2.2.3 The Calorimeters	16
67	2.2.4 The Muon Spectrometer	17
68	2.3 The ATLAS Trigger System	19
69	2.3.1 Level 1 Trigger	20
70	2.3.2 High-Level Trigger	20
71	3 The b-jet Trigger Signature in ATLAS	22
72	3.1 Trigger Efficiency	22

73	4 Event Simulation and Reconstruction	23
74	4.1 Event Generation	23
75	4.1.1 Parton Distribution Functions (PDFs)	23
76	4.1.2 Matrix Element Calculation	23
77	4.1.3 Parton Showers	23
78	4.1.4 Hadronisation	23
79	4.2 Detector Simulation	23
80	5 Stop searches in final states with jets and missing transverse energy	24
81	6 Results and Statistical Interpretations	25
82	Trigger	26
83	Bibliography	27

⁸⁴ List of Tables

⁸⁵	1.1 Forces and mediators described by the SM	4
---------------	--	---

⁸⁶ **List of Figures**

⁸⁷ 2.1	CERN Accelerator complex. The LHC is the last ring (dark grey line). Smaller machines are used for early-stage acceleration and also to provide beams for other experiments [1].	10
⁹⁰ 2.2	Cut-away view of the ATLAS detector. The dimensions of the detector are 25 m in height and 44 m in length. The overall weight of the detector is approximately 7000 tonnes [1].	11
⁹³ 2.3	The ATLAS magnet system.	12
⁹⁴ 2.4	The ATLAS Inner Detector	14
⁹⁵ 2.5	A computer generated image of the full calorimeter.	16
⁹⁶ 2.6	Cut-away view of the ATLAS muon system [2].	18
⁹⁷ 2.7	The ATLAS TDAQ system. L1Topo and FTK were being commissioned during 2015 and not used for the results shown in this thesis [3].	19

⁹⁹ Introduction

¹⁰⁰ Last thing to write

¹⁰¹ **Chapter 1**

¹⁰² **The Standard Model,
Supersymmetry, and the motivations
behind it**

¹⁰⁵

A theory is something nobody believes, except the person who made it. An experiment is something everybody believes, except the person who made it.

Albert Einstein

¹⁰⁶ The Standard Model (SM) of particle physics is an effective theory that aims to provide
¹⁰⁷ a general description of fundamental particles and the phenomena we see in nature, i. e.
¹⁰⁸ the way they interact. Unfortunately, our understanding of nature is still limited due to
¹⁰⁹ some opened question to which the SM is not able to answer to, yet.

¹¹⁰ In this chapter, an overview of the SM will be presented in Section 1.1 together with
¹¹¹ the limitations of such theory and some of the reasons behind the need of an extension.
¹¹² For the last decades theoretical physicsts have been trying to provide extensions to the
¹¹³ SM, the so-called beyond-the-SM theories. Among these, one of the most popular, Super-
¹¹⁴ symmetry which will be discussed in Section 1.2.

¹¹⁵ **1.1 The Standard Model**

¹¹⁶ The 20th century can be considered a quantum revolution. Several experiments led to
¹¹⁷ discoveries which were found to be, together with the formalised theory, a solid base of

¹¹⁸ the Standard Model of particle physics and our description of nature. Several particles
¹¹⁹ were predicted first by the SM and then experimentally observed e.g. the W and the Z
¹²⁰ bosons, the τ lepton, [4], and more recently the Higgs boson at the LHC discovered by
¹²¹ ATLAS [5] and CMS [6].

¹²² The SM lays on a Quantum Field Theory (QFT) where particles are treated like fields.
¹²³ It can describe three of the four fundamental forces; weak, electromagnetic, and strong.
¹²⁴ As of today, gravity is not considered in the SM. Sections 1.1.1 and 1.1.2 will be focused
¹²⁵ on the description of the fields together with the carriers of the information, and on the
¹²⁶ limitations that such theory implies, respectively.

¹²⁷ 1.1.1 Overview

¹²⁸ The most general classification of the particles within the SM can be made by means of
¹²⁹ spin. Fermions have half-integer spin values - and are usually referred to as matter -, and
¹³⁰ bosons have integer-spin values. A noteworthy subset of bosons is formed by the Spin-1
¹³¹ bosons (also known as gauge bosons). These can be considered the information carriers
¹³² or, in fact, the mediators of the forces.

¹³³ Fermions

¹³⁴ Six quarks and six leptons belong to the fermions family. In particular, fermions can be
¹³⁵ grouped into three generations. Each generation contains four particles; one up- and
¹³⁶ one down-type quark, one charged lepton and one neutral lepton. The masses of the
¹³⁷ charged leptons and quarks increase with the generation. The six quarks of the SM can
¹³⁸ be grouped into three doublets:

$$\begin{pmatrix} u \\ d \end{pmatrix}, \quad \begin{pmatrix} c \\ s \end{pmatrix}, \quad \begin{pmatrix} t \\ b \end{pmatrix}$$

¹³⁹ The up-type quarks (up, charm, top) have charge $+\frac{2}{3}e$ and the down-type quarks (down,
¹⁴⁰ strange, beauty/bottom) have charge $-\frac{1}{3}e$, where e is the electron charge. Quarks also
¹⁴¹ have another quantum number that can be seen as the analogue of the electric charge,
¹⁴² which is the colour charge. This can exist in three different states; "red", "green" and
¹⁴³ "blue". Moreover, as a consequence of *confinement*, which will be discussed later on in
¹⁴⁴ this section, quarks cannot exist as free particles. They rather group to form hadronic
¹⁴⁵ matter, also known as *hadrons*. There are two kinds of hadrons; mesons and baryons.
¹⁴⁶ Mesons are quark-antiquark systems, e.g. the pion, and baryons are three-quark system,

¹⁴⁷ e.g. protons and neutrons. Quarks and anti-quarks have a baryon number of $\frac{1}{3}$ and $-\frac{1}{3}$, respectively.

¹⁴⁹ There are six leptons and they can be classified in charged leptons (electron e , muon μ , tau τ) and neutral leptons (electron neutrino ν_e , muon neutrino ν_μ , tau neutrino ν_τ).

$$\begin{pmatrix} \nu_e \\ e^- \end{pmatrix}, \quad \begin{pmatrix} \nu_\mu \\ \mu^- \end{pmatrix}, \quad \begin{pmatrix} \nu_\tau \\ \tau^- \end{pmatrix}$$

¹⁵¹ Each lepton has a characteristic quantum number, called lepton number (L). Negatively ¹⁵² (positively) charged leptons have $L = -1$ ($L = 1$) and neutral leptons have $L = 0$. The ¹⁵³ lepton number is conserved in all the interactions.

¹⁵⁴ Forces of Nature

¹⁵⁵ Forces in the SM are described by gauge theories, where the interactions is mediated by a ¹⁵⁶ vector gauge boson. The electromagnetic force is described by Quantum ElectroDynam- ¹⁵⁷ ics (QED) and, as its mediator is the photon (γ) which couples to charged particles, it only ¹⁵⁸ affects charged leptons and quarks, whereas neutrinos cannot. They are instead affected ¹⁵⁹ by the weak force which is mediated by the bosons W^\pm and Z^0 . The weak interaction is ¹⁶⁰ associated with handedness (the projection of a particle spin onto its direction of motion). ¹⁶¹ Both leptons and quarks have left- and right-handed components. However, only the ¹⁶² left-handed (right-handed) component for neutrinos (anti-neutrinos) has been observed. ¹⁶³ This means that nature prefers to produce left-handed neutrinos and right-handed anti- ¹⁶⁴ neutrinos, which is the so-called parity violation. The strong interactions, mediated by ¹⁶⁵ the gluon (electrically neutral and massless), is described by Quantum ChromoDynamics ¹⁶⁶ (QCD). Table 1.1 summarises the forces described in the SM and their mediators' main ¹⁶⁷ characteristics. Finally, the gravitational force, which is believed to be mediated by the ¹⁶⁸ graviton, is not included in Table 1.1 as it is not part of the SM.

Table 1.1: Forces and mediators described by the SM

Force	Name	Symbol	Mass [GeV]	Charge
Electromagnetic	Photon	γ	0	0
Weak	W	W^\pm	80.398	$\pm e$
	Z	Z^0	91.188	0
Strong	Gluon	g	0	0

¹⁶⁹ **Symmetries and Gauge Groups**

¹⁷⁰ In 1915, the mathematician Emmy Noether (23 March 1882 – 14 April 1935) proved that
¹⁷¹ every differentiable symmetry of the action - defined as the integral over space of a Lag-
¹⁷² rangian density function - of a physical system has a corresponding conservation law.
¹⁷³ More generally, a symmetry is a property of a physical system. Under certain transform-
¹⁷⁴ ations this property is preserved.

¹⁷⁵ A gauge theory in QFT, is a theory in which the Lagrangian is invariant under a
¹⁷⁶ continuous group of local transformation. Group theory was then adopted to describe
¹⁷⁷ the symmetries conserved in the SM. The gauge group of the theory is the *Lie Group*.
¹⁷⁸ It contains all the transformations between possible gauges. The Lie algebra of group
¹⁷⁹ generators is therefore associated with any Lie group and for each group generator there
¹⁸⁰ emerges a corresponding field: the gauge field. The quanta of the gauge fields are called
¹⁸¹ *gauge bosons*.

¹⁸² The three SM interactions can therefore be mathematically described by the following:

$$U(1)_Y \otimes SU(2)_L \otimes SU(3)_C \quad (1.1)$$

¹⁸³ Here, Y is the weak hypercharge, used to estimate the correlation between the electric
¹⁸⁴ charge (Q) and the third component of the weak isospin (I_3) via the relation $Q = I_3 + Y/2$,
¹⁸⁵ where I_3 can either be $\pm 1/2$ or 0 for left-handed and right-handed particles, respectively;
¹⁸⁶ C the colour charge and L the left-handedness.

¹⁸⁷ As of today, we can describe three of the four forces of nature with group theory. QED
¹⁸⁸ is an Abelian gauge theory with $U(1)$ as symmetry group, with the electromagnetic four-
¹⁸⁹ potential as its gauge field and with the photon as its gauge boson [7]. The interactions
¹⁹⁰ between charged fermions occurs by the exchange of a massless photon.

¹⁹¹ The weak interaction and the strong interactions are non-Abelian gauge theories with
¹⁹² gauge groups $SU(2)$ and $SU(3)$, respectively. As a consequence of being non-Abelian
¹⁹³ the generators commutators are non-vanishing and therefore the gauge bosons can self-
¹⁹⁴ interact. The $SU(2)$ generators of the weak interaction are the massless gauge bosons
¹⁹⁵ $W_\mu^{\alpha=1,\dots,3}$ and, as mentioned earlier on in this chapter, they violate the parity by acting
¹⁹⁶ only on left-handed particles.

¹⁹⁷ The gauge bosons of $SU(3)_C$ are eight massless gluons, $G_\mu^{\alpha=1,\dots,8}$. The strong interac-
¹⁹⁸ tion does not distinguish left- and right-handed particles.

¹⁹⁹ **Electroweak Symmetry Breaking and the Higgs mechanism**

²⁰⁰ In 1979 Sheldon Glashow, Abdus Salam, and Steven Weinberg were awarded the No-
²⁰¹ bel Prize in Physics for their contributions to the so-called electroweak unification. In
²⁰² the mathematical description of the SM in 1.1 the electroweak interaction is described by
²⁰³ $U(1)_Y \otimes SU(2)_L$. Here, the gauge field associated with $U(1)_Y$ is the massless B_μ^0 . The elec-
²⁰⁴ troweak physical bosons W , Z and γ are related to the four unphysical bosons $W_\mu^{\alpha=1,\dots,3}$
²⁰⁵ and B_μ^0 . In particular, the field mixing of gauge bosons that gives birth to the physical
²⁰⁶ ones can be mathematically expressed by the following:

$$W_\mu^\pm = \frac{1}{\sqrt{2}} (W_\mu^1 \mp i W_\mu^2) \quad (1.2)$$

²⁰⁷

$$Z_\mu = B_\mu^0 \cos(\theta_W) + W_\mu^3 \sin(\theta_W) \quad (1.3)$$

²⁰⁸

$$A_\mu = -B_\mu^0 \sin(\theta_W) + W_\mu^3 \cos(\theta_W) \quad (1.4)$$

²⁰⁹ Here, θ_W is the so-called *Weinberg angle* which is the angle by which spontaneous
²¹⁰ symmetry breaking rotates the original W_μ^3 and B_μ^0 , producing the physical Z , and the
²¹¹ photon. It can be experimentally determined as the ratio of the electroweak coupling
²¹² constants g and g' using the relation $\tan(\theta_W) = g/g'$. Finally, the Quarks that interact
²¹³ through weak interaction are mixtures of SM eigenstates as described by the CKM matrix
²¹⁴ [8].

²¹⁵ **1.1.2 Limitations of the Standard Model**

²¹⁶ bla

²¹⁷ **1.2 Supersymmetry**

²¹⁸ **1.2.1 Why SUSY?**

²¹⁹ bla

²²⁰ **1.2.2 Minimal Supersymmetric Standard Model**

²²¹ bla

222 1.2.3 R-parity SUSY

223 bla

224 1.2.4 Simplified models

225 bla

226 1.2.5 Phenomenological MSSM

227 bla

²²⁸ **Chapter 2**

²²⁹ **The ATLAS Experiment at the LHC**

²³⁰ ATLAS (A Toroidal LHC ApparatuS) is one of the four main experiments (ATLAS, CMS,
²³¹ ALICE, LHCb) taking data at a center-of-mass energy of 13 TeV using beams delivered by
²³² the Large Hadron Collider (LHC). In this chapter an overview of the LHC will be given
²³³ in Section 2.1, then the ATLAS detector will be described in Section 2.2, and finally the
²³⁴ Trigger system, used to cleverly store the data, will be described in Section 2.3. A more
²³⁵ in-depth description of the Trigger algorithms I have been involved in will be given in
²³⁶ Chapter 3.

²³⁷ **2.1 The LHC**

²³⁸ As of today, the LHC is the world's largest and most powerful particle accelerator. It
²³⁹ was designed to help answer some of the fundamental open questions in particle phys-
²⁴⁰ ics by colliding protons at an unprecedented energy and luminosity. It is located at the
²⁴¹ European Organisation for Nuclear Research (CERN), in the Geneva area, at a depth ran-
²⁴² ging from 50 to 175 metres underground. It consists of a 27-kilometre ring made of su-
²⁴³ perconducting magnets, and inside it two high-energy particle beams travel in opposite
²⁴⁴ directions and in separate beam pipes.

²⁴⁵ The beams are guided around the ring by a strong magnetic field generated by coils -
²⁴⁶ made of special electric cables - that can operate in a superconducting regime. 1232 super-
²⁴⁷ conducting dipole and 392 quadrupole magnets, with an average magnetic field of 8.3 T,
²⁴⁸ are employed and kept at a temperature below 1.7 K, in order to preserve their supercon-
²⁴⁹ ducting properties. The formers are used to bend the beams and the latters to keep them
²⁵⁰ focused while they get accelerated.

²⁵¹ The collider first went live on September 2008 even though, due to a magnet quench

252 incident that damaged over 50 superconducting magnets, it has been operational since
 253 November 2009 when low-energy beams circulated in the tunnel for the first time since
 254 the incident. This also marked the start of the main research programme and the begin-
 255 ning of the so-called Run 1: first operational run (2009 - 2013).

256 Performance of the LHC

257 In June 2015 the LHC restarted delivering physics data, after a two-year break, the so-
 258 called Long Shutdown 1 (LS1), during which the magnets were upgraded to handle the
 259 current required to circulate 7-TeV beams. It was the beginning of the so-called Run 2 -
 260 second operational run (2015-2018) - during which LHC has collided up to 10^{11} bunches
 261 of protons every 25 ns at the design luminosity - the highest luminosity the detector was
 262 designed to cope with - of $2 \cdot 10^{34} \text{ cm}^{-2} \text{s}^{-1}$. The definition of the luminosity is:

$$\mathcal{L} = f \frac{n_b N_1 N_2}{4\pi\sigma_x\sigma_y} \quad (2.1)$$

263 where N_1 and N_2 are the number of protons per bunch in each of the colliding beams, f
 264 is the revolution frequency of the bunch collisions, n_b the number of proton per bunch,
 265 and σ_x and σ_y are the horizontal and vertical dimensions of the beam. The luminosity is
 266 strictly related to the number of collisions occurring during a certain experiment via the
 267 following:

$$\mathcal{N}_{\text{event}} = \mathcal{L}\sigma_{\text{event}} \quad (2.2)$$

268 where σ_{event} is the cross section of the process under investigation. It has not only collided
 269 protons but also heavy ions, in particular lead nuclei at $\sqrt{s_{NN}} = 5.02 \text{ TeV}$, at a luminosity
 270 of $10^{27} \text{ cm}^{-2} \text{s}^{-1}$ [9].

271 Acceleration stages

272 Before reaching the maximum energy, the proton beams are accelerated by smaller ac-
 273 celerators through various stages. Figure 2.1 shows a sketch of the CERN's accelerator
 274 complex. It all begins at the linear accelerator LINAC 2. Here protons are accelerated up
 275 to 50 MeV, and then injected in the Proton Synchrotron Booster (PSB) where they reach
 276 1.4 GeV. The next stage is the Proton Synchrotron (PS), which boosts the beams up to 25
 277 GeV and then the Super Proton Synchrotron (SPS) makes them reach energies up to 450
 278 GeV. Eventually, the beams are injected in bunches with a 25 ns spacing into the LHC,
 279 where they travel in opposite directions, while they are accelerated to up to 13 TeV. Once

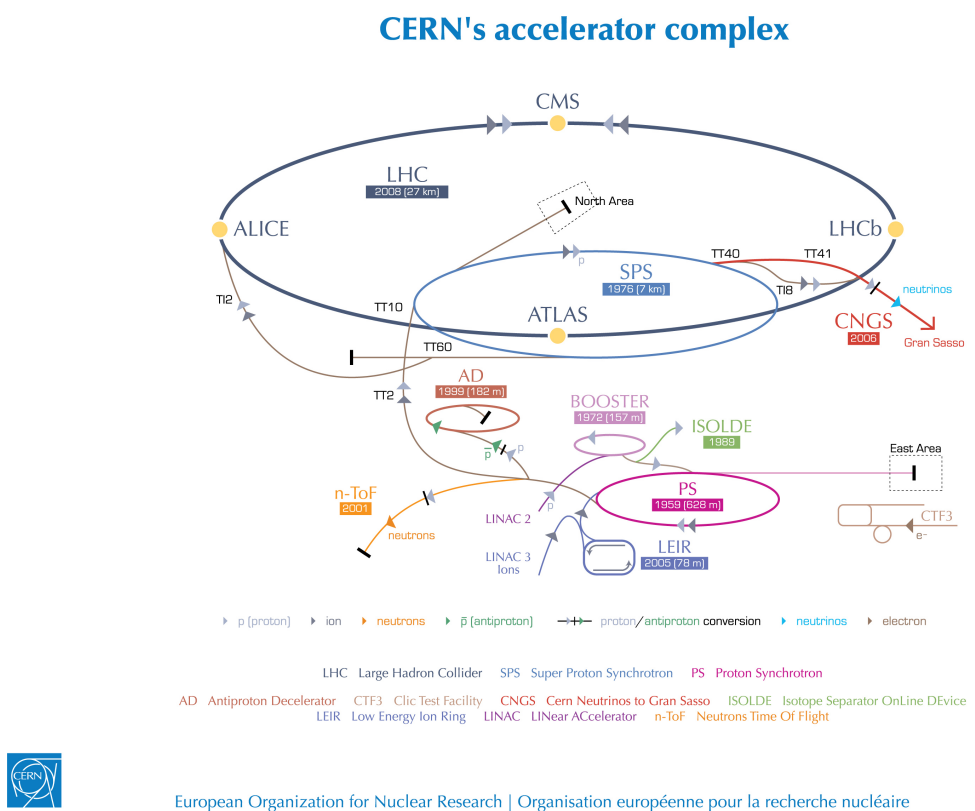


Figure 2.1: CERN Accelerator complex. The LHC is the last ring (dark grey line). Smaller machines are used for early-stage acceleration and also to provide beams for other experiments [1].

280 the bunches reach the maximum energy, they are made collide at four different points,
281 inside four experiments around the ring [10].

282 The heavy ion beams acceleration procedure is slightly different. Their journey starts
283 at LINAC 3 first, and the Low Energy Ion Ring (LEIR) then, before they make their way
284 into the PS where they follow the same path as the protons [10].

285 The four large detectors on the collision points are; the multi-purpose detectors A Tor-
286 oidal LHC ApparatuS (ATLAS), and Compact Muon Solenoid (CMS) [11], Large Hadron
287 Collider beauty (LHCb) [12], which focuses on flavour physics, and A Large Ion Collider
288 Experiment (ALICE) [13] which specialises in heavy ion physics. The *big four* are not the
289 only experiments at the CERN's accelerator complex. There also are smaller experiments
290 based at the the four caverns about the collision points e.g. TOTEM, LHCf and MoEDAL,
291 but this will not be discussed any further in this thesis.

292 2.2 The ATLAS Detector

293 ATLAS is a general-purpose detector designed to collect data with the highest luminosity
294 provided by the LHC. It is located at CERN's Point 1 cavern and it measures about 45 m in

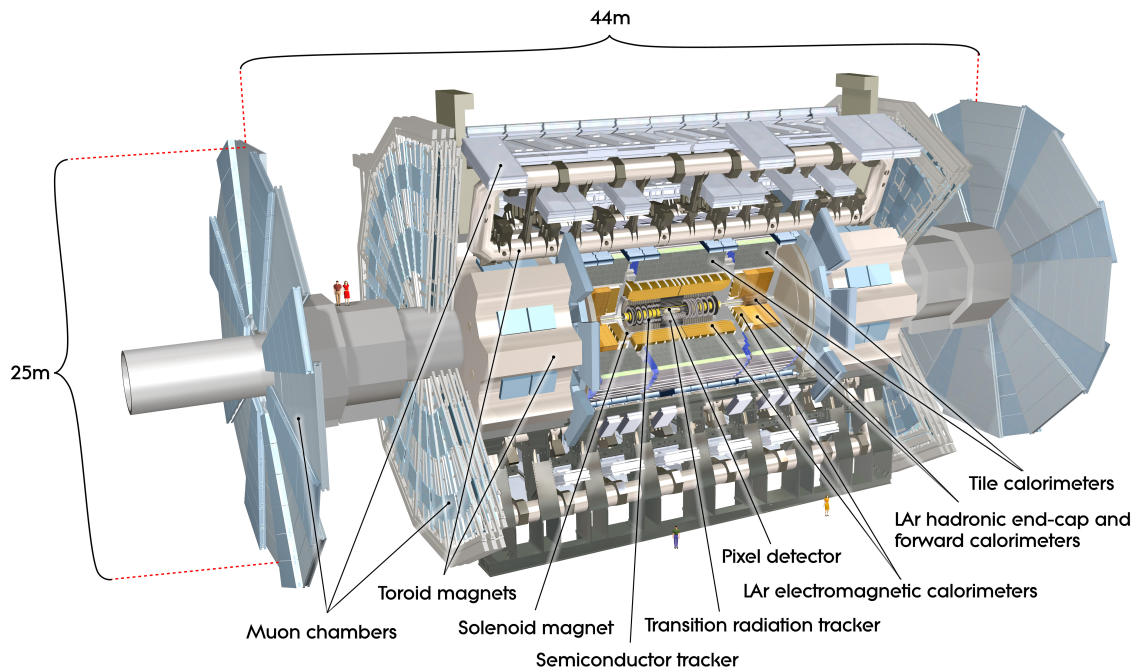


Figure 2.2: Cut-away view of the ATLAS detector. The dimensions of the detector are 25 m in height and 44 m in length. The overall weight of the detector is approximately 7000 tonnes [1].

length and 25 m in diameter. It has a forward-backward symmetric cylindrical geometry with respect to the interaction point and it is designed to reconstruct and measure physics objects such as electrons, muons, photons and hadronic jets. Its design was optimised to be as sensitive as possible to the discovery of the Higgs boson and beyond-the-Standard-Model (BSM) physics. In fact, thanks to the other sub-systems, ATLAS is able to observe all possible decay products by covering nearly 4π steradians of solid angle.

In Figure 2.2 a cut-away view of ATLAS with all its components is shown. The inner-most layer is the Inner Detector (ID) which is the core of the tracking system and consists of a Pixel, a Silicon micro-strip tracker (SCT), and a Transition Radiation Tracker (TRT). It is submerged in a 2 T magnetic field, generated by a thin superconducting solenoid, which bends all the charged particles' trajectories allowing transverse momentum measurement. The electromagnetic and hadronic calorimeters form the next layer and they are both used to perform precise energy measurements of photons, electrons, and hadronic jets. Finally, the outermost layer corresponds to the Muon Spectrometer (MS) which, together with the ID, enclosed in a toroidal magnetic field, allows precise measurement of momentum and position of muons. These sub-detectors will be discussed in more detail in the following sections.

312 **The ATLAS coordinate system**

313 A coordinate system is taken on for the spatial definition of the sub-systems and kin-
314 ematic measurement of physics processes. Such system is defined starting from the in-
315 teraction point, defined as the origin. The z -axis is defined by the beam direction and the
316 $x - y$ plan, as transverse to the beam direction.

317 A quantity, known as pseudorapidity, (η), is defined to describe the angle of a particle
318 coming out of the collision, with respect to the beam axis:

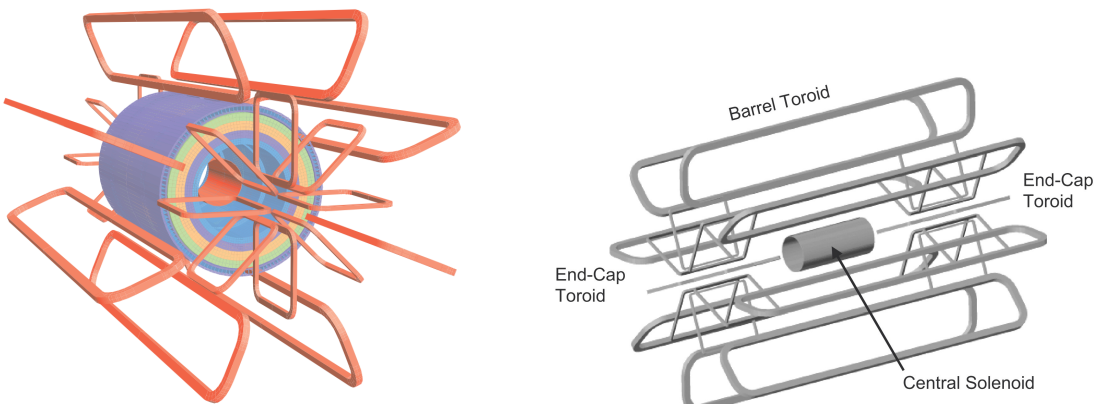
$$\eta \equiv -\ln(\tan(\theta/2))$$

319 Here θ is the polar angle. The azimuthal angle, ϕ , is defined around the beam axis and
320 the polar angle. In the (η, ϕ) space a distance ΔR can be therefore defined as

$$\Delta R = \sqrt{\Delta\eta^2 + \Delta\phi^2}$$

321 where $\Delta\eta$ and $\Delta\phi$ are the differences in pseudorapidity and azimuthal angle between
322 any two considered objects. A central and a forward region of pseudorapidity are also
323 defined such that the detector components are described as part of the *barrel* if they belong
324 to the former or as part of the *end-caps* if they belong to the latter.

325 **2.2.1 The Magnet System**



(a) Geometry of magnet windings and tile calorimeter steel. The eight barrel toroid coils, with the end-cap coils interleaved are visible. The solenoid winding lies inside the calorimeter volume [2].

(b) Schematic view of the superconducting magnets [14].

Figure 2.3: The ATLAS magnet system.

³²⁶ The ATLAS magnet system, 26 m long with a 22 m diameter, generates the magnetic
³²⁷ field needed to bend the trajectories of charged particles in order to perform momentum
³²⁸ measurement. Figure 2.3a and 2.3b show the geometry of the system and its compo-
³²⁹ nents, which are made of NbTi - superconducting material - and will be described in the
³³⁰ following paragraphs.

³³¹ **The Central Solenoid**

³³² With an axial length of 5.8 m, an inner radius of 2.46 m, and an outer radius of 2.56 m, the
³³³ central solenoid magnet is located between the ID and the ECAL. Its function is to bend
³³⁴ the charged particles that go through the ID and it is aligned on the beam axis providing
³³⁵ a 2 T axial magnetic field that allows accurate momentum measurement up to 100 GeV
³³⁶ [14].

³³⁷ **The Barrel and the End-cap Toroids**

³³⁸ Figure 2.3b displays the toroid magnetic system that surrounds the calorimeters. With
³³⁹ its cylindrical shape this component consists of a barrel and two end-caps toroids, each
³⁴⁰ with eight superconducting coils. The system allows accurate measurement of muon
³⁴¹ momenta using a magnetic field of approximately 0.5 T (barrel) for the central regions
³⁴² and 1 T (end-cap) for the end-cap regions, respectively, which bends the particles in the
³⁴³ θ direction.

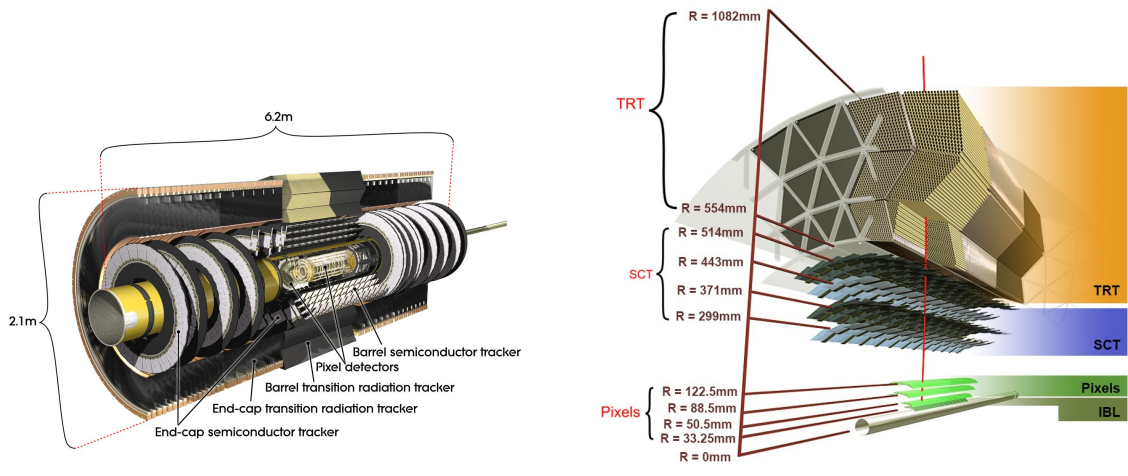
³⁴⁴ **2.2.2 The Inner Detector**

³⁴⁵ The Inner Detector (ID) [15] is the innermost component of the ATLAS detector i. e. the
³⁴⁶ nearest sub-detector to the interaction region and it is used to reconstruct charged particle
³⁴⁷ tracks used in the selection of physics objects. In fact, it allows robust track reconstruc-
³⁴⁸ tion, with accurate impact parameter resolution ($\sim 20\mu m$) and precise primary and sec-
³⁴⁹ ondary vertex reconstruction for charged particles (tracks) above 500 MeV and within
³⁵⁰ $|\eta| < 2.5$.

³⁵¹ The ID is comprised of independent and concentric sub-systems, which are all shown
³⁵² in Figure 2.4:

- ³⁵³ • Insertable B-Layer (IBL):

³⁵⁴ innermost Pixel Detector layer added during ATLAS Run-2 upgrade (2013/2014)
³⁵⁵ to improve vertexing and impact parameter reconstruction;



(a) Overview of the ATLAS ID with labels and dimensions.

(b) Diagram of the ATLAS ID and its sub-detectors.

Figure 2.4: The ATLAS Inner Detector

356 • Silicon Pixel Tracker (Pixel):

357 made of silicon pixel layers and used mainly for reconstructing both the primary
358 and secondary vertices in an event;

359 • SemiConductor Tracker (SCT):

360 comprised of silicon microstrip layers; thanks to its resolution ($17 \times 580 \mu\text{m}$) it can
361 accurately measure particle momenta;

362 • Transition Radiation Tracker (TRT):

363 final layer comprised of various layers of gaseous straw tube elements surrounded
364 by transition radiation material.

365 These sub-detectors will be discussed in the following sections.

366 **IBL**

367 The IBL [16] is the innermost Pixel Detector layer as shown in Figure 2.4b. It is comprised
368 of 6M channels and each pixel measures $50 \times 250 \mu\text{m}$. Its resolution is $8 \times 40 \mu\text{m}$. The
369 addition of this new layer brought a considerable improvement on the performance of the
370 Pixel Detector by enhancing the quality of impact parameter reconstruction of tracks. In
371 particular, this was achieved by improving the vertex finding efficiency and the tagging
372 of bottom-quark-initiated jets (b -jets) which, in case of a B-layer failure, can be restored
373 by the IBL. Besides these improvements, the IBL insertion allowed ATLAS to better cope

³⁷⁴ with high luminosity effects such as the increase in event pile-up, which leads to high
³⁷⁵ occupancy and read-out inefficiency.

³⁷⁶ **Pixel**

³⁷⁷ The Pixel detector is comprised of 1750 identical sensorchip-hybrid modules, each cover-
³⁷⁸ ing an active area of 16.4×60.8 mm. The total number of modules correspond to roughly
³⁷⁹ 80 million semiconductor silicon pixels. The nominal pixel size is $50 \mu\text{m}$ in the ϕ direction
³⁸⁰ and $400 \mu\text{m}$ in the barrel region, along the z -axis (beam axis) [17]. The reason why such a
³⁸¹ large amount of pixels is employed is justified by the need to cope with the high lumino-
³⁸² sity in ATLAS. The silicon pixel detector measures 48.4 cm in diameter and 6.2 m in length
³⁸³ providing a pseudorapidity coverage of $|\eta| < 2.5$. Figure 2.4b shows the three concentric
³⁸⁴ barrel layers placed at 50.5 mm, 88.5 mm and 122.5 mm respectively. Furthermore, the
³⁸⁵ Pixel detector is made of six disk layers, three for each forward region, such that when a
³⁸⁶ charged particle crosses the layers it will generate a signal at least in three space points.
³⁸⁷ The fine granularity of such detector allows accurate measurement and precise vertex
³⁸⁸ reconstruction, as it provides a more accurate position measurement as a large detection
³⁸⁹ area is available. In particular, it has a resolution of $10 \times 115 \mu\text{m}$.

³⁹⁰ **SCT**

³⁹¹ The SCT is made of 4088 modules of silicon micro-strip detectors arranged in four con-
³⁹² centric barrel layers. It is mainly used for precise momentum reconstruction over a range
³⁹³ $|\eta| < 2.5$ and it was designed for precision measurement of the position using four points
³⁹⁴ (corresponding to eight silicon layers), obtained as track hits when crossing the layers.
³⁹⁵ Figure 2.4b shows the structure of the SCT with its four concentric barrel layers with
³⁹⁶ radii ranging from 299 mm to 514 mm and two end-cap layers. Each module has an in-
³⁹⁷ trinsic resolution of $17 \mu\text{m}$ in the $R - \phi$ direction and $580 \mu\text{m}$ in the z direction. As the
³⁹⁸ SCT is further away from the beam-pipe than the Pixel detector, it has to cope with re-
³⁹⁹ duced particle density. This allows for reduced granularity maintaining the same level of
⁴⁰⁰ performance of the Pixel detector: SCT can use ~ 6.3 million read-out channels.

⁴⁰¹ **TRT**

⁴⁰² The last and outermost of the sub-systems in the ID is the TRT. It is a gaseous detector
⁴⁰³ which consists of 4 mm diameter straw tubes wound from a multilayer film reinforced
⁴⁰⁴ with carbon fibers and containing a $30 \mu\text{m}$ gold plated tungsten wire in the center. The

straw is filled with a gas mixture of 70% Xe, 27% CO₂ and 3% O₂ [18]. As shown in Figure 2.4b, its section consists of three concentric layers with radii ranging from 544 mm to 1082 mm, each of which has 32 modules containing approximately 50,000 straws, 1.44 m in length, aligned parallel to the beam direction with independent read-out at both ends. Both end-cap sections are divided into 14 wheels, with roughly 320,000 straws in the R-direction. The average 36 hits per track in the central region of the TRT allow continuous tracking to enhance pattern recognition and momentum resolution in the $|\eta| < 2.5$ region. It also improves the p_T resolution for longer tracks.

2.2.3 The Calorimeters

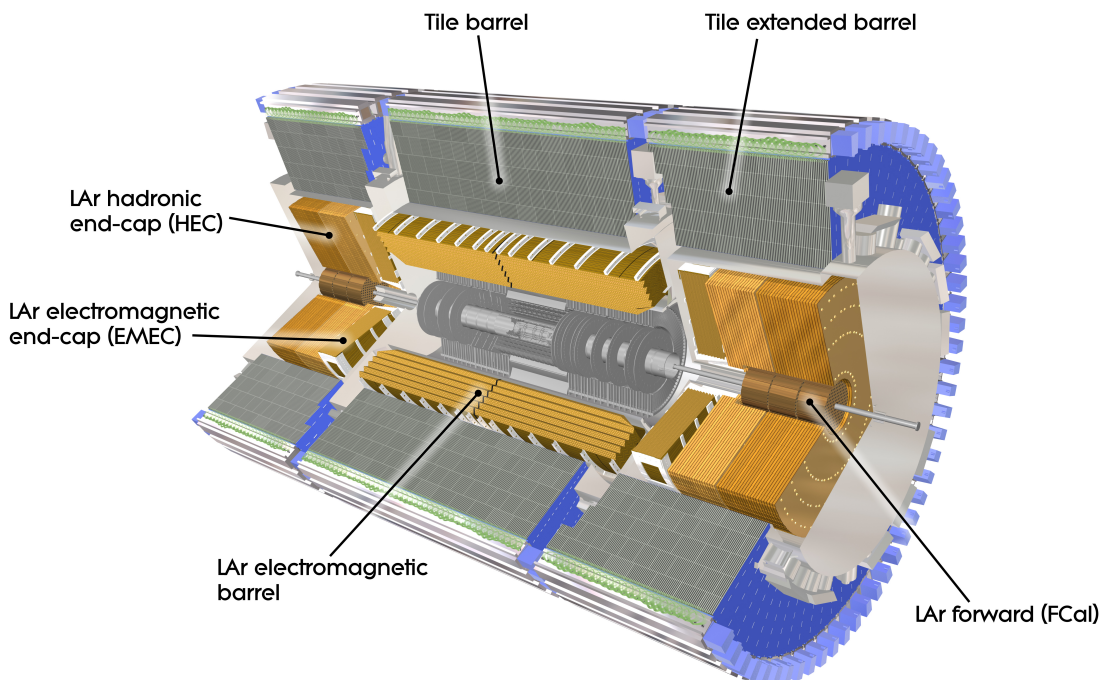


Figure 2.5: A computer generated image of the full calorimeter.

The ATLAS Calorimeter system, shown in Figure 2.5, is comprised of two main subsystems; the electromagnetic calorimeter (ECAL) and hadronic calorimeter (HCAL), which are designed to stop and measure the energy of electromagnetic-interacting and hadronic particles respectively. The combination of the two provides full coverage in ϕ and $|\eta| < 4.95$. Particles slow down and lose energy generating showers when crossing different layers. The ECAL is comprised of one barrel and two end-cap sectors employing liquid Argon (LAr). The showers hereby develop as electrons pairs which are then collected. The HCAL is also comprised of one barrel and two end-cap sectors. The sensors

⁴²² in the barrel of the HCAL are tiles of scintillating plastic whereas LAr is employed for
⁴²³ the end-cap. A forward region, the closest possible to the beam, is covered by a LAr for-
⁴²⁴ ward calorimeter (FCal). The LAr and Tile Calorimeter will be briefly discussed in the
⁴²⁵ following paragraphs.

⁴²⁶ The Liquid Argon Calorimeters

⁴²⁷ The ECAL is comprised of multiple layers of liquid Argon (LAr) sampler and lead ab-
⁴²⁸ sorber. The choice of its accordion-geometry design brought two main advantages; full
⁴²⁹ ϕ coverage with no non-interactive regions (no cracks); fast extraction of signals coming
⁴³⁰ from both front or rear end of the electrodes. It is made of two half-barrel wheels, both
⁴³¹ placed in the barrel cryostat, that provide a pseudorapidity coverage up to $|\eta| < 1.475$
⁴³² and two end-cap detectors providing $1.375 \leq |\eta| \leq 3.20$ coverage in two end-cap cryo-
⁴³³ stats. The junction between the barrel and end cap components defines the crack region
⁴³⁴ and any signal coming from the crack region is therefore discarded.

⁴³⁵ In the $|\eta| < 1.8$ region there is an additional layer, placed at the front of the calori-
⁴³⁶ meter, that is made of a thin (0.5 cm in the end-cap and 1.1 cm in the barrel) LAr layer
⁴³⁷ with no absorber [19]. This additional layer was designed to correct for the energy lost,
⁴³⁸ as particles enter the calorimeter, by taking a measurement just before the majority of the
⁴³⁹ electromagnetic shower is developed.

⁴⁴⁰ The Tile calorimeter

⁴⁴¹ The main purpose of the hadronic calorimeter is to measure the energy of hadronic
⁴⁴² showers. It is built employing steel and scintillating tiles coupled to optical fibres which
⁴⁴³ are read out by photo-multipliers. As shown in Figure 2.5, the HCAL is made up of three
⁴⁴⁴ cylinders; a central barrel, 5.64 m long covering a region $|\eta| < 1.0$, and two extended
⁴⁴⁵ barrel, 2.91 m long covering a reigon $0.8 < |\eta| < 1.7$. Each cylinder is made up of 64
⁴⁴⁶ modules and each module is in turn made up of three layers. Ultimately, the smallest
⁴⁴⁷ section of the calorimeter module is a cell with a $\Delta\phi \times \Delta\eta = 0.1 \times 0.1$ granularity for the
⁴⁴⁸ two innermost layers and $\Delta\phi \times \Delta\eta = 0.2 \times 0.1$ for the outermost one.

⁴⁴⁹ 2.2.4 The Muon Spectrometer

⁴⁵⁰ The MS [20], shown in Figure 2.6, is the outermost sub-system of the whole ATLAS de-
⁴⁵¹ tector. As such, it surrounds the calorimeters and its main function is to perform precision

452 measurement of muons momenta. The deflection of muon tracks employing large super-
 453 conducting air-core toroid magnets and high-precision tracking chambers is at the heart
 454 of such high precision measurement.

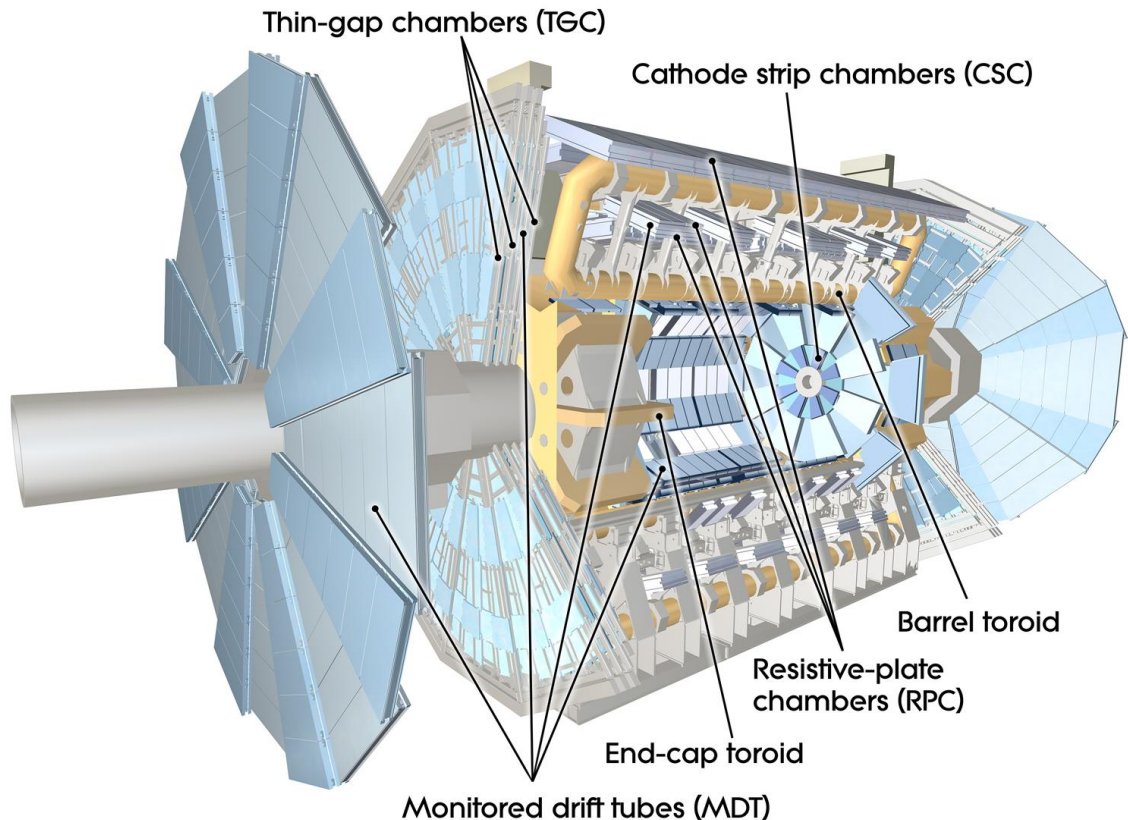


Figure 2.6: Cut-away view of the ATLAS muon system [2].

455 The MS is comprised of one large barrel toroid, covering the region $|\eta| \leq 1.4$, and two
 456 end-cap toroids, covering $1.6 < |\eta| \leq 2.7$ which are employed together to achieve the
 457 track-bending effect wanted. The magnitude of the magnetic field in the barrel, generated
 458 by eight large superconducting coils, ranges from 0.5 to 2 T.

459 Around the beam axis, three cylindrical layers make way for the chambers, placed in
 460 planes perpendicular to the beam, used to measure tracks.

461 Monitored Drift Chambers (MDTs) are employed over most of the pseudorapidity
 462 range to provide precision measurement of track coordinates in the bending direction.
 463 Cathode Strip Chambers (CSCs) are instead employed at large pseudorapidity ($2 < |\eta| <$
 464 2.7). Finally, in the end-cap regions Thin-Gap Chambers (TGCs) together with Resistive-
 465 Plate Chambers (RPCs) are dedicated to the Trigger System discussed in Section 2.3.

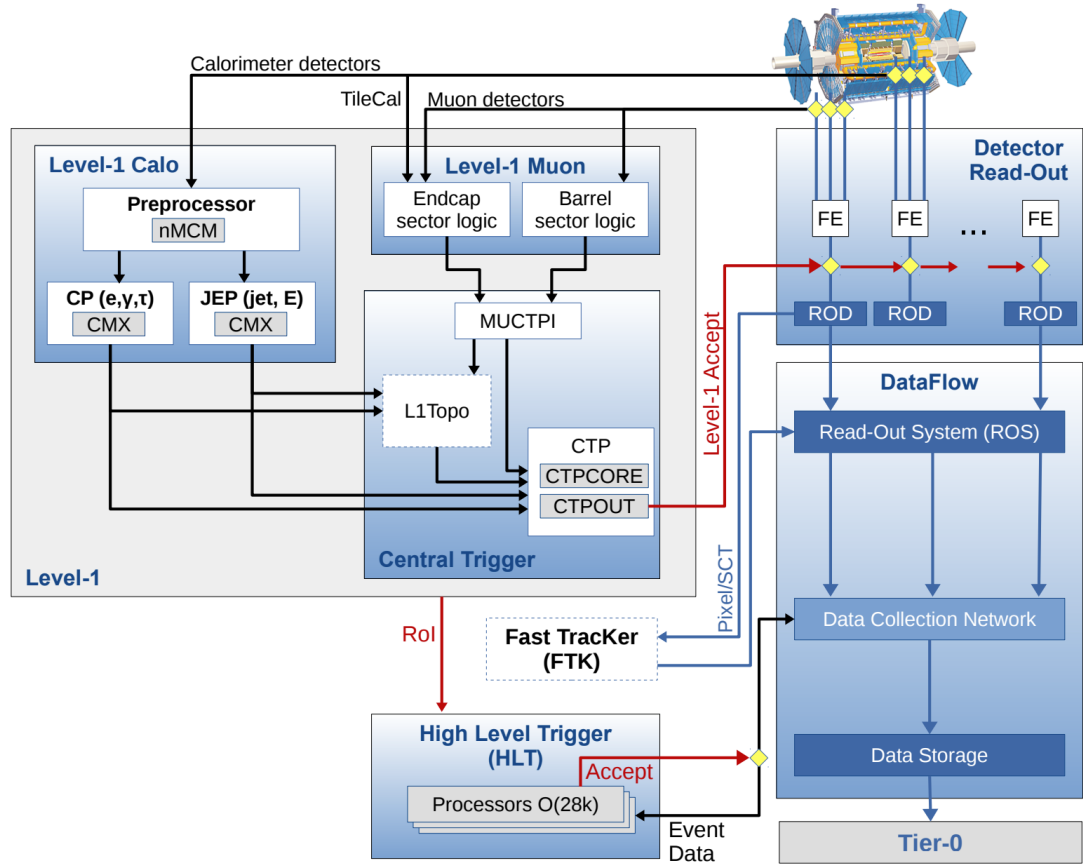


Figure 2.7: The ATLAS TDAQ system. L1Topo and FTK were being commissioned during 2015 and not used for the results shown in this thesis [3].

466 2.3 The ATLAS Trigger System

467 The ATLAS Trigger System is at the heart of data taking. It is an essential component of
 468 any nuclear or particle physics experiment since it is responsible for deciding whether
 469 or not to store an event for later study [3]. The ATLAS Trigger system is employed to
 470 reduce the event rate from ~ 40 MHz¹ bunch-crossing² to ~ 200 Hz which corresponds
 471 to roughly 300 MB/s.

472 The Trigger and Data Acquisition (TDAQ) system shown in Figure 2.7 consists of
 473 a hardware-based first level trigger (L1) and a software-based high-level trigger (HLT).
 474 The L1 trigger decision is formed by the Central Trigger Processor (CTP), which receives
 475 inputs from the L1 calorimeter (L1Calo) and L1 muon (L1Muon) triggers. The first level
 476 (L1), which was designed to perform the first selection step, is a hardware-based system

¹The LHC delivers beams with a bunch-spacing of 25 ns.

²The term bunch-crossing is hereby used when referring to a collision between two bunches of protons.

Since only a certain fraction of the total momentum carried by each proton contributes to the collision, an average number of interactions per bunch-crossing, $\langle \mu \rangle$ is used.

477 that uses information from the calorimeter and muon subdetectors. It also defines the so-
 478 called Regions of Interest (RoIs) within the detector to be investigated by the next level
 479 trigger, the HLT. Additionally, a Fast TracKer (FTK) system [21] (not yet installed) will
 480 provide global ID track reconstruction at the L1 trigger rate using lookup tables stored
 481 in custom associative memory chips for the pattern recognition. The FPGA-based track
 482 fitter will perform a fast linear fit and the tracks are made available to the HLT. This
 483 system will allow the use of tracks at much higher event rates in the HLT than is currently
 484 affordable using CPU systems. However, the upgrade of the ATLAS trigger will not be
 485 discussed any further.

486 In the next sections the L1 and HLT will be briefly described.

487 2.3.1 Level 1 Trigger

488 The Level 1 Trigger identifies Regions of Interest (RoIs)³ and passes these to HLT which
 489 will perform further investigations. Furthermore, in order to decide whether or not the
 490 event processing will continue, L1 selection uses only information coming from some
 491 parts of the detector to keep the input rate to a maximum of 100 kHz. L1 is implemented
 492 in fast custom electronics to keep the latency⁴ below 2.5 μ s. Event data from other sub-
 493 syststem are temporarily stored in memories whilst L1 decision is taken.

494 The L1 topological trigger (L1-Topo) [22] is feeded with energy and direction inform-
 495 ation, about the objects found by the L1 calorimeter and the muon trigger, which will be
 496 processed by dedicated algorithms implemented in its own FPGAs. However, due to the
 497 100 kHz read-out rate, not all the information collected by L1-Topo will be sent to the
 498 HLT, but only part of it. In order to properly seed the ROI-guided HLT reconstruction,
 499 specific objects in combination with the correct topological criteria must be employed.

500 2.3.2 High-Level Trigger

501 The HLT is used to reduce the output rate down to 1 kHz and it has a \sim 200 ms average
 502 decision time. Events that pass L1 trigger are then processed by the HLT using finer-
 503 granularity calorimeter information, precision measurements from the MS and tracking
 504 information from the ID. The HLT reconstruction can be run within RoIs identified at L1
 505 or a so-called full-scan on the full detector can be performed. The track reconstruction in
 506 the Inner Detector is an essential component of the trigger decision in the HLT and it will

³ $\eta - \phi$ regions where event features have been found by the L1 selection process.

⁴Time needed by an electric signal to get to the front-end electronics.

⁵⁰⁷ be discussed more in detail in Chapter 3

508 **Chapter 3**

509 **The b -jet Trigger Signature in ATLAS**

510 In this chapter the monitor and performance of the bottom-quark-initiated jet (b -jet) sig-
511 nature trigger, this being the author’s “technical/qualification task” to become a qualified
512 member of the experiment, will be discussed. The efficiencies of some of the Run 2 b -jet
513 triggers were evaluated using 3.8 fb^{-1} of pp collisions data collected in 2015 with 25 ns
514 bunch-spacing.

515 The qualification task

516 **3.1 Trigger Efficiency**

517 **Chapter 4**

518 **Event Simulation and Reconstruction**

519 bla bla bla

520 **4.1 Event Generation**

521 bla bla

522 **4.1.1 Parton Distribution Functions (PDFs)**

523 bla bla bla

524 **4.1.2 Matrix Element Calculation**

525 bla bla bla

526 **4.1.3 Parton Showers**

527 bla bla bla

528 **4.1.4 Hadronisation**

529 bla bla bla

530 **4.2 Detector Simulation**

531 bla bla bla

⁵³² **Chapter 5**

⁵³³ **Stop searches in final states with jets
and missing transverse energy**

⁵³⁵ **Chapter 6**

⁵³⁶ **Results and Statistical Interpretations**

⁵³⁷ Trigger

⁵³⁸ bla vlas bla

Bibliography

- 539 [1] C. Lefèvre, *The CERN accelerator complex.*, <http://cds.cern.ch/record/1260465>.
 540 viii, 10, 11
- 542 [2] ATLAS Collaboration, *The ATLAS experiment at the CERN Large Hadron Collider*,
 543 Journal of Instrumentation **3** no. 08, (2008) S08003.
 544 <http://stacks.iop.org/1748-0221/3/i=08/a=S08003>. viii, 12, 18
- 545 [3] A. Collaboration, *Performance of the ATLAS Trigger System in 2015*, Eur. Phys. J. **C77**
 546 (2017), [arXiv:1611.09661 \[hep-ex\]](https://arxiv.org/abs/hep-ph/1611.09661). viii, 19
- 547 [4] M. Herrero, *The Standard Model.*, <https://arxiv.org/abs/hep-ph/9812242>. 3
- 548 [5] ATLAS Collaboration, *Observation of a New Particle in the Search for the Standard
 549 Model Higgs Boson with the ATLAS Detector at the LHC*, Phys.Lett. **B716** (2012),
 550 [arXiv:1207.7214 \[hep-ex\]](https://arxiv.org/abs/hep-ph/1207.7214). 3
- 551 [6] CMS Collaboration, *Observation of a new boson at a mass of 125 GeV with the CMS
 552 experiment at the LHC*, Phys.Lett. **B716** (2012), [arXiv:1207.7235 \[hep-ex\]](https://arxiv.org/abs/hep-ph/1207.7235). 3
- 553 [7] A. Pich, *The Standard Model of Electroweak Interactions*, [arXiv:1201.0537 \[hep-ph\]](https://arxiv.org/abs/hep-ph/1201.0537).
 554 5
- 555 [8] K. A. Olive et al. (Particle Data Group), *Review of Particle Physics*, Chin.Phys. C **38**(9)
 556 (2014). 6
- 557 [9] J.M. Jowett, M. Schaumann, R. Alemany, R. Bruce, M. Giovannozzi, P. Hermes, W.
 558 Hofle, M. Lamont, T. Mertens, S. Redaelli, J. Uythoven, J. Wenninger, *The 2015
 559 Heavy-Ion Run of the LHC*,
 560 <http://accelconf.web.cern.ch/accelconf/ipac2016/papers/tupmw027.pdf>. 9
- 561 [10] O. S. Brüning, P. Collier, P. Lebrun, S. Myers, R. Ostojic, J. Poole and P. Proudlock,
 562 *LHC Design Report*, <https://cds.cern.ch/record/782076>. 10

- 563 [11] CMS Collaboration, *The CMS experiment at the CERN LHC*, Journal of
 564 Instrumentation **3** no. 08, (2008) S08004.
 565 <http://stacks.iop.org/1748-0221/3/i=08/a=S08004>. 10
- 566 [12] LHCb Collaboration, et. al, *The LHCb Detector at the LHC*, JINST (2008). 10
- 567 [13] ALICE Collaboration, *The ALICE experiment at the CERN LHC*, Journal of
 568 Instrumentation **3** no. 08, (2008) S08002.
 569 <http://stacks.iop.org/1748-0221/3/i=08/a=S08002>. 10
- 570 [14] A. Yamamoto, Y. Makida, R. Ruber, Y. Doi, T. Haruyama, F. Haug, H. ten Kate,
 571 M. Kawai, T. Kondo, Y. Kondo, J. Metselaar, S. Mizumaki, G. Olesen, O. Pavlov,
 572 S. Ravat, E. Sbrissa, K. Tanaka, T. Taylor, and H. Yamaoka, *The ATLAS central*
 573 *solenoid*, Nuclear Instruments and Methods in Physics Research Section A:
 574 Accelerators, Spectrometers, Detectors and Associated Equipment **584** no. 1, (2008)
 575 53 – 74.
 576 <http://www.sciencedirect.com/science/article/pii/S0168900207020414>. 12,
 577 13
- 578 [15] ATLAS Collaboration, *The ATLAS Inner Detector commissioning and calibration*, Eur.
 579 Phys. JC**70**, arXiv:1004.5293. 13
- 580 [16] ATLAS Collaboration, *ATLAS Insertable B-Layer Technical Design Report*,
 581 <https://cds.cern.ch/record/1291633>. 14
- 582 [17] G. A. et al., *ATLAS pixel detector electronics and sensors*, Journal of Instrumentation **3**
 583 no. 07, (2008) P07007. <http://stacks.iop.org/1748-0221/3/i=07/a=P07007>. 15
- 584 [18] A. Bingül, *The ATLAS TRT and its Performance at LHC*, Journal of Physics:
 585 Conference Series **347** no. 1, (2012) 012025.
 586 <http://iopscience.iop.org/article/10.1088/1742-6596/347/1/012025/meta>.
 587 16
- 588 [19] ATLAS Collaboration, *ATLAS liquid-argon calorimeter: Technical Design Report*,
 589 <https://cds.cern.ch/record/331061>. 17
- 590 [20] ATLAS Collaboration, *ATLAS muon spectrometer: Technical design report*,
 591 <https://cds.cern.ch/record/331068>. 17
- 592 [21] ATLAS Collaboration, *Fast TracKer (FTK) Technical Design Report*,
 593 <https://cds.cern.ch/record/1552953>. 20

-
- 594 [22] E. Simoni, *The Topological Processor for the future ATLAS Level-1 Trigger: from design to*
595 *commissioning*, [arXiv:1406.4316](https://arxiv.org/abs/1406.4316). 20